PAPER

Check for updates

Preparation and lithium storage of core–shell honeycomb-like Co₃O₄@C microspheres†

Linhe Yu,[a] Qihao Yang,[a] Guozhen Zhu [ID] *[a] and Renchao Che [ID] *[bc]

Core–shell honeycomb-like Co₃O₄@C microspheres were synthesized *via* a facile solvothermal method and subsequent annealing treatment under an argon atmosphere. Owing to the core–shell honeycomb-like structure, a long cycling life was achieved (a high reversible specific capacity of 318.9 mA h g^{-1} was maintained at 5C after 1000 cycles). Benefiting from the coated carbon layers, excellent rate capability was realized (a reversible specific capacity as high as 332.6 mA h g^{-1} was still retained at 10C). The design of core–shell honeycomb-like microspheres provides a new idea for the development of anode materials for high-performance lithium-ion batteries.

Introduction

Developing rechargeable batteries with high energy density is urgently needed to meet the growing demand for electric vehicles and smart electrical grids.[1,2] Lithium-ion batteries are a promising rechargeable battery technology. The anode material plays a significant role in enhancing the electrochemical performance of lithium-ion batteries. Common anode materials mainly include lithium metal materials, carbon materials[3] (graphite, hard carbon, soft carbon, *etc.*), titania-based oxide materials (titanium dioxide, lithium titanate, *etc.*), and alloy materials (silicon, tin, *etc.*). However, further applications have been strictly limited by their poor security, low theoretical specific capacity, and large volume expansion. Thus, there is an urgent need to explore high-specific-capacity anode materials.

Transition metal oxides have been widely studied due to their high theoretical specific capacity, low cost, environmental friendliness, and rich resources.[4–6] However, the electrochemical performance of transition metal oxide suffers due to their poor conductivity, low initial cycle coulomb efficiency, and poor cycling stability.[7–10] Various methods have been proposed to enhance their conductivity. Cu₀.₆Ni₀.₄Co₂O₄ nanowires were successfully synthesized, which exhibited more excellent electrochemical performance than CuCo₂O₄ and NiCo₂O₄ due to the doping of copper. A reversible specific capacity of 880 mA h g^{-1} was maintained after 50 cycles at 50 mA g^{-1}.[11] Co₃O₄/SWCNT-M13 was reported to have a high specific capacity of 1283.5 mA h g^{-1} at 2 A g^{-1}, showing excellent rate capability.[12] A

hierarchical hollow Co–Mo–O NCs/rGO composite was synthesized, and a high reversible specific capacity of 333 mA h g^{-1} was achieved at 5 A g^{-1} because of the hierarchical hollow structure and graphene, exhibiting superior rate performance.[13] Moreover, excellent cycling stability has been achieved by controlling the size[14–16] and regulating the morphology of transition metal oxides.[17–20] CoO with a compact-nanobox structure was prepared, which demonstrated excellent cycling stability (90.4% capacity retention after 100 cycles) due to the compact configuration and internal cavity.[21] In addition, designing a porous structure is an effective method for improving the structural stability of transition metal oxides.[22–26] Co₃O₄@TiO₂ with a mesoporous hollow nanocage structure was prepared. Owing to the design of the mesoporous hollow nanocage structure, Co₃O₄@TiO₂ showed excellent cycling stability. A discharge capacity of 787.5 mA h g^{-1} was obtained after 200 cycles.[27] The crystal structure of Co₃O₄ is shown in Fig. S1,† which is spinel structured and crystallizes in the tetragonal $I4_1md$ space group. CoO₄ tetrahedra were formed by the bond between Co^{2+} and four O^{2-} atoms, which shared corners with twelve equivalent CoO₆ octahedra. CoO₆ octahedra were formed by the bond between Co^{3+} and six O^{2-} atoms, which shared corners with six equivalent CoO₄ tetrahedra and edges with six equivalent CoO₆ octahedra.

Herein, core–shell honeycomb-like Co₃O₄@C microspheres were prepared using the facile solvothermal method and annealing treatment in an argon atmosphere. Owing to the core–shell honeycomb-like structure, the specific surface area was greatly increased. Moreover, the volume change was greatly alleviated by the abundant pores distributed throughout the microspheres during the long-term charge and discharge processes. Furthermore, the transmission of electrons was accelerated by the carbon layers coated on the surface of the Co₃O₄ microspheres. As a result, long cycling stability and

[a]Institute of Advanced Materials, Jiangxi Normal University, Nanchang 330022, P. R. China. E-mail: zhuguozhen@jxnu.edu.cn; rcche@fudan.edu.cn

[b]Laboratory of Advanced Materials, Shanghai Key Lab of Molecular Catalysis and Innovative Materials, Fudan University, Shanghai 200438, P. R. China

[c]Department of Materials Science, Fudan University, Shanghai 200438, P. R. China

excellent rate capability of the core–shell honeycomb-like $Co_3O_4@C$ microspheres were achieved.

Experimental section

Materials

Cobalt chloride, 1,3,5-benzoic acid, sodium dodecyl benzene sulfonate, 2-methylimidazole, *N,N*-dimethyl bromide methyl formamide, and absolute ethanol were purchased from Sinopharm Chemical Reagent Co., Ltd. All the chemical reagents were used without further purification.

Synthesis of solid Co_3O_4 microspheres

The synthetic process of solid Co_3O_4 microspheres is shown in Fig. 1. Firstly, 0.100 g cobalt chloride, 0.105 g 1,3,5-benzoic acid, and 0.050 g 2-methylimidazole were mixed with 30 mL *N,N*-dimethyl bromide methyl formamide and stirred magnetically for 1 h at 45 °C. Secondly, the mixed solution was transferred to a stainless steel sealed autoclave and maintained for 12 h at 180 °C. Thirdly, the obtained solution was centrifuged and rinsed 6 times each with deionized water and ethanol and dried in a vacuum oven for 24 h at 80 °C to obtain the precursor powders. Finally, solid Co_3O_4 microspheres (denoted as SCo_3O_4) were synthesized by annealing at 800 °C for 12 h in air.

Synthesis of core–shell honeycomb-like $Co_3O_4@C$ microspheres

The synthetic process of core–shell honeycomb-like $Co_3O_4@C$ microspheres is shown in Fig. 1. Firstly, 0.100 g cobalt chloride, 0.105 g 1,3,5-benzoic acid, 0.040 g 2-methylimidazole, 0.100 g cetyltrimethyl ammonium bromide, and 0.005 g sodium dodecyl benzene sulfonate were mixed with 35 mL *N,N*-dimethyl bromide methyl formamide and stirred magnetically for 1 h at 45 °C. Secondly, the mixed solution was poured into a stainless steel sealed autoclave and maintained for 20 h at 180 °C. Thirdly, the obtained solution was centrifuged and rinsed 6 times each with deionized water and ethanol and dried in a vacuum oven for 24 h at 80 °C to obtain the precursor powders. Finally, the core–shell honeycomb-like $Co_3O_4@C$

microspheres (denoted as $CSHCo_3O_4@C$) were fabricated by annealing at 800 °C for 12 h in an argon atmosphere.

Synthesis of flower-like Co_3O_4

The synthetic process of flower-like Co_3O_4 is shown in Fig. 1. Firstly, 0.100 g cobalt chloride, 0.105 g 1,3,5-benzoic acid, 0.040 g 2-methylimidazole, 0.100 g cetyltrimethyl ammonium bromide, and 0.005 g sodium cetylbenzene sulfonate were mixed with 35 mL *N,N*-dimethyl bromide methyl formamide and stirred magnetically for 1 h at 45 °C. Secondly, the mixed solution was poured into a stainless steel sealed autoclave and maintained for 18 h at 180 °C. Thirdly, the obtained solution was centrifuged and rinsed 6 times each with deionized water and ethanol and dried in a vacuum oven for 24 h at 80 °C to obtain the flower-like Co_3O_4 microsphere precursor powders. Finally, the flower-like Co_3O_4 microspheres (denoted as FCo_3O_4) were prepared by annealing at 800 °C for 12 h in air.

Material characterization

The phase composition and crystal structure were characterized by X-ray diffraction (Bruker D8 Advance). The micromorphology was analyzed by field-emission scanning electron microscopy (Hitachi, S-4800). The specific surface area was tested on a specific surface analyzer (ASAP2020). The coated carbon layers were identified *via* Raman spectrometry (Renishaw inVia Reflex). The coated carbon contents were calculated by thermogravimetric measurement (Pyris 1TGA) from 20 °C to 800 °C in air with a heating rate of 5 °C min^{-1}.

Measurement of electrochemical performance

Firstly, the active substance, acetylene black, and polyvinylidene fluoride were mixed evenly in a mass ratio of 8 : 1 : 1. Secondly, the mixed powders were mixed with *N*-methylpyrrolidone and stirred for 1 h to prepare a slurry with good fluidity. Thirdly, the slurry was evenly covered on the surface of copper foil using an automatic coating machine to obtain a film of 90 μm thickness, which was subsequently dried in a vacuum oven for 24 h at 80 °C. Fourthly, the film was punched into discs with a diameter of
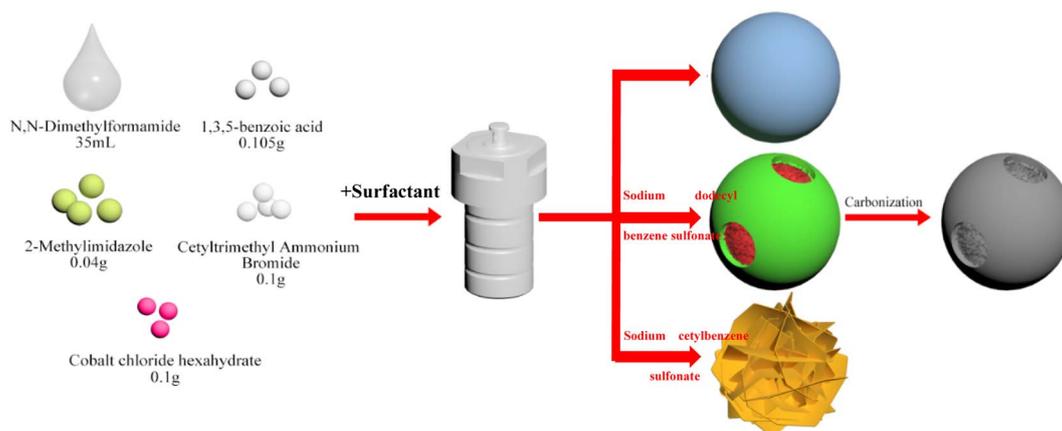

Fig. 1 Synthetic process of SCo_3O_4, $CSHCo_3O_4@C$, and FCo_3O_4.

16 mm and dried in a vacuum oven for 12 h at 80 °C. Finally, the disc, LiFP$_6$, microporous polypropylene film, and metal lithium sheet were assembled into a button battery in a glovebox filled with argon gas. The cycling stability and rate performance were evaluated using a Land battery measurement system (CT2001A). Cyclic voltammetry and electrochemical impedance spectroscopy were performed on an electrochemical workstation (CHI604D).

Results and discussion

Fig. 2a presents the XRD patterns of the SCo$_3$O$_4$, CSHCo$_3$O$_4$@C, and FCo$_3$O$_4$ microspheres, illustrating that all the diffraction peaks match well with the standard PDF card (No. 43-1003, Co$_3$O$_4$). The diffraction peaks located at 19°, 31.3°, 36.8°, 38.5°, 44.8°, 55.7°, 59.4°, and 65.2° could be ascribed to the crystal planes of (111), (220), (311), (222), (400), (422), (511), and (440), respectively, demonstrating that pure SCo$_3$O$_4$, CSHCo$_3$O$_4$@C, and FCo$_3$O$_4$ microspheres were synthesized successfully. No diffraction peak of carbon was observed, indicating that the carbon layers coated on the surface of the CSHCo$_3$O$_4$ microspheres were amorphous. Raman spectroscopy was performed to identify that the carbon layers were coated on the CSHCo$_3$O$_4$ microspheres (Fig. 2b). Compared with the SCo$_3$O$_4$ and FCo$_3$O$_4$ microspheres, the CSHCo$_3$O$_4$ microspheres showed two more peaks at 1310 cm^{-1} and 1599 cm^{-1} in their Raman spectra, which correspond to the D-band and G-band peaks of carbon. The D-band peak is caused by incomplete graphite microcrystals, structural defects, edge unsaturation, and carbon atoms. The G-band peak represents the integrity of the sp^2 hybrid bond structure in the graphite structure of carbon.[28,29] The I_D/I_G ratio was greater than 1, indicating that the coated carbon layers had defects. The carbon content of the CSHCo$_3$O$_4$@C microspheres was about 4.42 wt% (Fig. S2†).

Fig. 3 shows SEM images of the CSHCo$_3$O$_4$@C microspheres. Good dispersion was observed (Fig. 3a). An obvious core–shell honeycomb-like structure was observed (Fig. 3c, S3a, b and S4†) with a few holes distributed on the surface of the shell. Abundant interconnected nanopores were uniformly distributed throughout the core (Fig. 3c), which provided a path extending in all directions for the transmission of the

electrolyte.[30,31] A 50 nm-thick pore wall ensured the stability of the honeycomb structure during the long-term charging/discharging processes (Fig. 3d). In contrast, the SCo$_3$O$_4$ and FCo$_3$O$_4$ microspheres were synthesized via the facile solvothermal method (Fig. 4a and b). The sizes of the SCo$_3$O$_4$ microspheres ranged from 1 μm to 4 μm, and they were bonded together, which was not conducive to improving the lithium storage performance. The FCo$_3$O$_4$ microspheres comprised nanosheets with a thickness of 100 nm. The pores between nanosheets guarantee full contract between the active substance and the electrolyte. Fig. S3c† presents an HRTEM image of the CSHCo$_3$O$_4$@C microspheres. The clearly visible lattice stripes indicate the good crystallinity of the CSHCo$_3$O$_4$@C microspheres, and the crystal plane spacing of 0.35 nm could be ascribed to the crystal plane of (440). The porous structure of the CSHCo$_3$O$_4$@C microspheres was further confirmed using a specific surface analyzer (Fig. S5†). The specific surface area of the CSHCo$_3$O$_4$@C microspheres (58.3 m^2 g^{-1}) was significantly greater than that of the SCo$_3$O$_4$ microspheres (21.2 m^2 g^{-1}) due to the honeycomb and core–shell structure. The pores distributed throughout the microspheres and the gap between the core and shell were conducive to improving the specific surface area.

Fig. S6† presents the 1st, 2nd, and 150th charge/discharge curves of the CSHCo$_3$O$_4$@C, SCo$_3$O$_4$, and FCo$_3$O$_4$ microspheres at 0.2C. The gap between the discharge curves of the 2nd and 150th cycles of the CSHCo$_3$O$_4$@C microspheres was significantly smaller than those of the SCo$_3$O$_4$ and FCo$_3$O$_4$ microspheres, showing the better cycling reversibility of the CSHCo$_3$O$_4$@C microspheres. The cycling stability curves of the CSHCo$_3$O$_4$@C, SCo$_3$O$_4$, and FCo$_3$O$_4$ microspheres are shown in Fig. 5a. The initial reversible specific capacity of the CSHCo$_3$O$_4$@C microspheres was as high as 1269.3 mA h g^{-1} at 0.2C, which was slightly higher than that of SCo$_3$O$_4$ (1226.7 mA h g^{-1}) and FCo$_3$O$_4$ (1232.5 mA h g^{-1}). A high reversible specific capacity of 1091.2 mA h g^{-1} was maintained after 150 cycles, indicating the excellent cycling stability of the CSHCo$_3$O$_4$@C microspheres. In contrast, the reversible specific capacity of the SCo$_3$O$_4$ microspheres attenuated to 87.5 mA h g^{-1} after 150 cycles, showing poor cycling stability. The CSHCo$_3$O$_4$@C microspheres showed the highest coulombic efficiency during
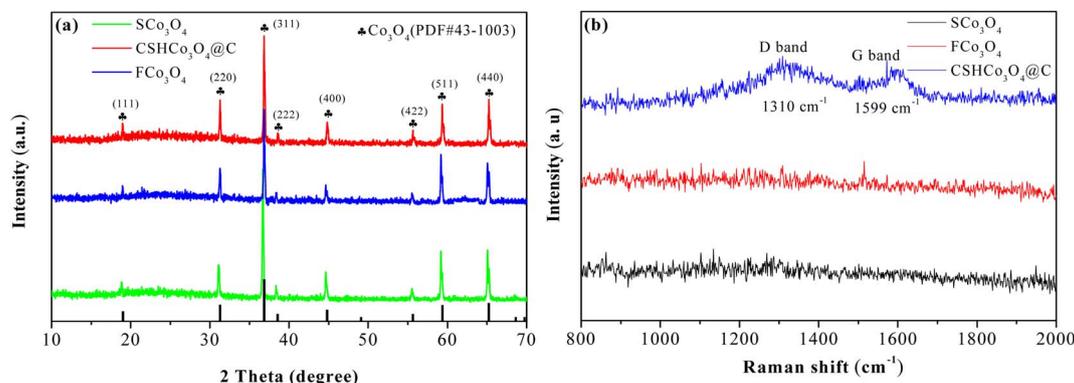

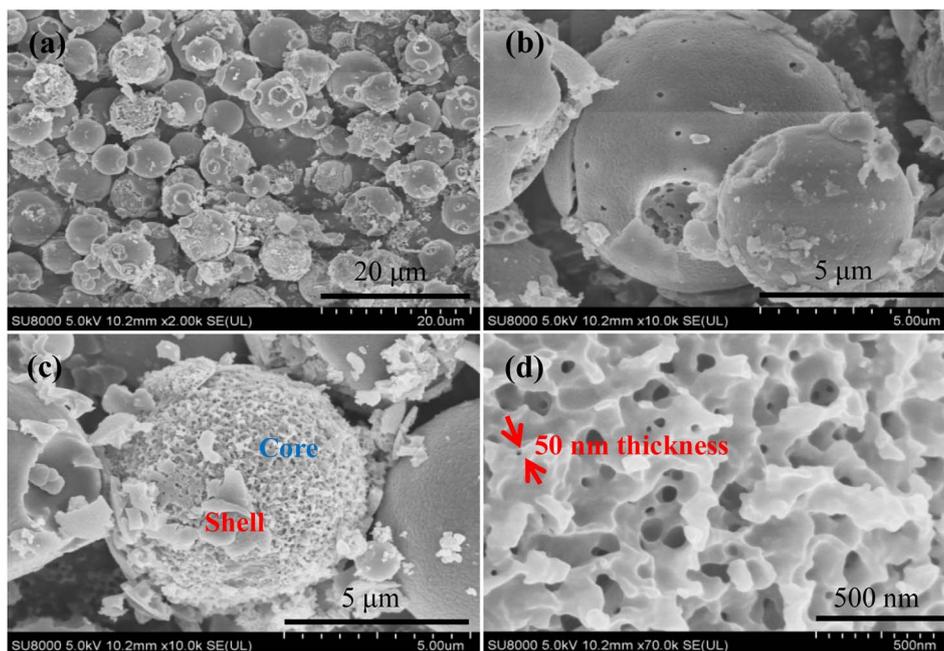**Fig. 2** (a) XRD patterns and (b) Raman spectra of the SCo$_3$O$_4$, CSHCo$_3$O$_4$@C and FCo$_3$O$_4$ microspheres.

Fig. 3 SEM images of the $CSHCo_3O_4@C$ microspheres (a) low magnification, (b) low magnification shell surface, (c) low magnification core surface, (d) high magnification core surface.

cycling, except at the initial cycle, among the three prepared microspheres (Fig. S7†). A comparison with previous reports using similar materials but different structures is shown in Table S2.† The $CSHCo_3O_4@C$ microspheres exhibited better cycling stability than the other reported cobalt oxide materials.

To further identify the superior cycling stability of the $CSHCo_3O_4@C$ microspheres, the current density was increased to 5C, and the cycles were increased to 1000 (Fig. S8†). A high reversible specific capacity of 318.9 mA h g^{-1} was still retained after 1000 cycles, and the coulombic efficiency was more than 90% during the 1000 cycles except for the first cycle (73.6%), illustrating the excellent cycling stability of the $CSHCo_3O_4@C$ microspheres. Fig. 5b shows the rate capability of the $CSHCo_3O_4@C$, SCo_3O_4, and FCo_3O_4 microspheres. The reversible specific capacities of the $CSHCo_3O_4@C$ microspheres were

the highest among the three microspheres at different current densities. Due to electrode polarization, the reversible specific capacity decreased continuously with the increase in current density. The reversible specific capacities of the $CSHCo_3O_4@C$ microspheres were 1216.5 mA h g^{-1}, 1074.6 mA h g^{-1}, 884.3 mA h g^{-1}, 805.7 mA h g^{-1}, 530.5 mA h g^{-1}, and 332.6 mA h g^{-1} at 0.2C, 1C, 2C, 3C, 5C, and 10C, respectively, and a reversible specific capacity of 1113.8 mA h g^{-1} was achieved when the current density recovered to 0.2C. In sharp contrast, the reversible specific capacities of the SCo_3O_4 microspheres were 993.6 mA h g^{-1}, 863.9 mA h g^{-1}, 583.5 mA h g^{-1}, 367.1 mA h g^{-1}, 159.6 mA h g^{-1}, and 68.7 mA h g^{-1} at 0.2C, 1C, 2C, 3C, 5C, and 10C, respectively, and a reversible specific capacity of 867.6 mA h g^{-1} was obtained when the current density recovered to 0.2C. Furthermore, the $CSHCo_3O_4@C$ microspheres showed the most
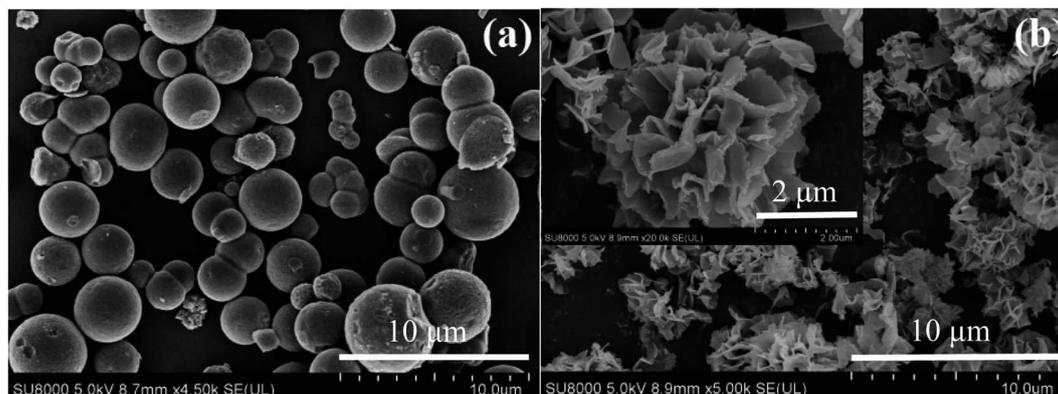

Fig. 4 SEM images of the (a) SCo_3O_4 and (b) FCo_3O_4 microspheres.
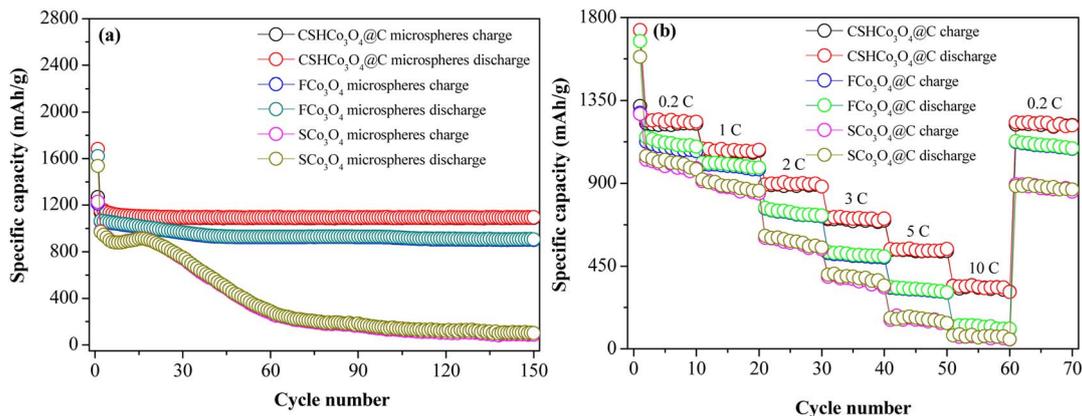
Fig. 5 (a) Cycling stability and (b) rate performance of the CSHCo₃O₄@C, SCo₃O₄, and FCo₃O₄ microspheres.

excellent rate capability among the reported Co₃O₄ materials (Table S1†).

The cyclic voltammetry curves of the first three cycles of the CSHCo₃O₄@C microspheres are shown in Fig. 6a. The voltage ranged from 0 V to 3.0 V, and the scan rate was set to 0.1 mV s⁻¹. In the first cathodic scan process, the reduction peak located at 1.38 V corresponded to the reduction of CO_3O_4 to CoO, and the reduction peak at 0.88 V was ascribed to the reduction of CoO to Co and the formation of solid electrolyte interphase films. The oxidation peaks at 1.61 V and 2.16 V were related to the oxidation of Co to CoO and CoO to Co₃O₄ during the first anodic scan process, respectively. After the first cathodic scan process, the reduction peak shifted to 0.92 V, and the intensity of the reduction peak weakened, showing the irreversible formation of solid electrolyte interphase films.[32,33] The cyclic voltammetry curves of the last two cycles almost coincided, indicating the good electrochemical reversibility and distinguished cycling stability of the CSHCo₃O₄@C microspheres.[34,35]

The electrochemical impedance spectroscopy results of the CSHCo₃O₄@C, SCo₃O₄, and FCo₃O₄ microspheres are shown in Fig. 6b. The semicircle represents the charge transfer

resistance, and the straight line represents lithium-ion diffusion. The CSHCo₃O₄@C microspheres exhibited the smallest semicircle and minimum straight line slope among the prepared three microspheres, implying the lowest charge transfer resistance and the fastest lithium ion diffusion of the CSHCo₃O₄@C microspheres. An equivalent circuit diagram of the EIS is illustrated in Fig. 6b, and the EIS data were fitted. The CSHCo₃O₄@C microspheres exhibited the lowest R_{ct} among the three microspheres, demonstrating the excellent rate capability of the CSHCo₃O₄@C microspheres. The resistance values of the CSHCo₃O₄@C, SCo₃O₄, and FCo₃O₄ microspheres are shown in Table S3.† The CSHCo₃O₄@C microspheres showed the lowest R_{ct} among the three microspheres. The $σ$ values of the CSHCo₃O₄@C, SCo₃O₄, and FCo₃O₄ microspheres calculated using the Warburg coefficient are shown in Fig. S9.† Based on the formula $D = R^2T^2/2A^2n^4F^4C^2σ^2$, the lithium-ion diffusion coefficient increases with a decrease in $σ$ value. The CSHCo₃O₄@C microspheres exhibited the lowest $σ$ value among the three microspheres, thus showing the highest Li-ion diffusion coefficient and the strongest Li-ion diffusion capability. The 1ˢᵗ, 2ⁿᵈ, and 150ᵗʰ electrochemical impedance spectroscopy curves
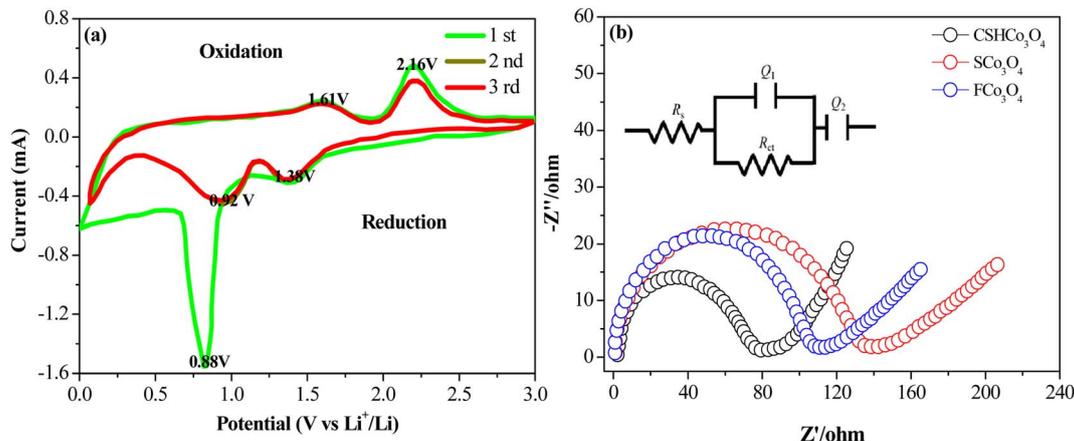

Fig. 6 (a) Cyclic voltammetry curves of the first 3 cycles of the CSHCo₃O₄@C microspheres and (b) electrochemical impedance spectroscopy results of the CSHCo₃O₄@C, SCo₃O₄, and FCo₃O₄ microspheres.
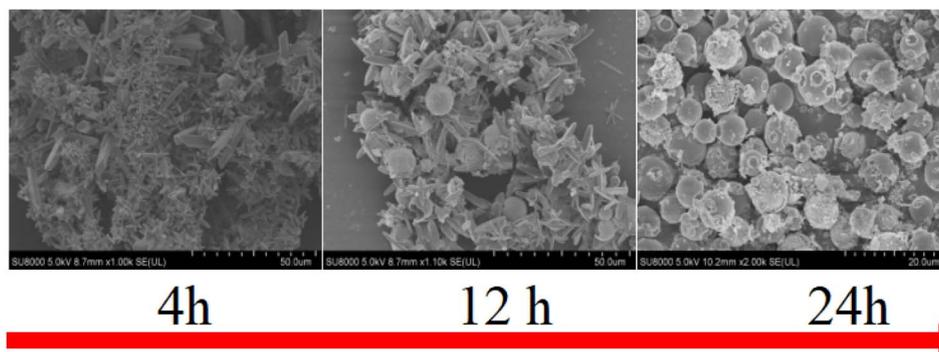
Fig. 7 Formation process of the $CSHCo_3O_4$ microspheres.

of the $CSHCo_3O_4$@C microspheres are shown in Fig. S10.† The resistance values during cycling are presented in Table S4.† The R_{ct} first decreases and then increases during cycling because a stable and compact SEI film is formed on the surface of the anode material, which is conducive to electron transfer. In the later stage of cycling, the SEI film on the electrode surface is damaged, and the thickness also increases, leading to an increase in electrochemical impedance.

The formation process of the $CSHCo_3O_4$ microspheres was analysed by observing the SEM images taken under different solvothermal times (Fig. 7). Nanorods and microrods of different sizes were formed at 4 h. Due to the induction of sodium dodecyl benzene sulfonate, some nanorods and microrods were assembled into microspheres at 12 h. The nanorods and microrods were all transformed into microspheres, and these microspheres were then transformed into $CSHCo_3O_4$ microspheres at 24 h.

The long cycling stability of the $CSHCo_3O_4$@C microspheres could be ascribed to the core–shell honeycomb-like structure. The abundant nanopores distributed throughout the microspheres were conducive to increasing the specific surface area, providing more active sites for the full electrochemical reaction, and improving the reversible specific capacity.[36,37] Furthermore, the cavity between the core and shell and the nanopores distributed throughout the microspheres were beneficial in relieving the volume expansion from the long-term charge and discharge processes, thereby enhancing the cycling stability of the microspheres.[38,39] In addition, the coated carbon layers could improve the conductivity of the microspheres, promote the transfer of electrons, and alleviate electrode polarization, thereby improving the rate capability.[40,41]

Conclusion

In conclusion, we synthesized $CSHCo_3O_4$@C microspheres. The uniform and continuous nanopores distributed throughout the microspheres provided abundant pathways for the penetration of the electrolyte, ensuring full contact between the active substance and electrolyte. Meanwhile, the volume expansion during the repeated lithiation and delithiation processes could be effectively inhibited by the various nanopores, thereby achieving long cycling life (a reversible specific capacity as high

as 318.9 mA h g^{-1} was maintained at 5C after 1000 cycles). Furthermore, the conductivity of the Co_3O_4 microspheres was significantly enhanced, the transfer speed of electrons was greatly improved, and excellent rate capability was obtained (a high reversible specific capacity of 332.6 mA h g^{-1} was maintained at 10C).

Conflicts of interest

The authors declare no competing financial interest.

Acknowledgements

References

1 Q. Q. Lu, A. Omar, L. Ding, *et al.*, A facile method to stabilize sodium metal anodes towards high-performance sodium batteries, *J. Mater. Chem. A*, 2021, **9**, 9038–9047.

2 L. X. Liu, J. W. Wang, S. Oswald, *et al.*, Decoding of Oxygen Network Distortion in a Layered High-Rate Anode by *In Situ* Investigation of a Single Microelectrode, *ACS Nano*, 2020, **14**(9), 11753–11764.

3 Q. Q. Lu, Y. L. Jie, X. Q. Meng, *et al.*, Carbon materials for stable Li metal anodes: Challenges, solutions, and outlook, *Carbon Energy*, 2021, **3**, 957–975.

4 M. B. Zheng, H. Tang, L. L. Li, *et al.*, Hierarchically Nanostructured Transition Metal Oxides for Lithium-Ion Batteries, *Adv. Sci.*, 2018, **5**(3), 1700592.

5 Q. B. Yun, L. X. Li, Z. N. Hu, *et al.*, Layered Transition Metal Dichalcogenide-Based Nanomaterials for Electrochemical Energy Storage, *Adv. Mater.*, 2019, **32**(1), 1903826.

6 R. Zhang, X. X. Huang, D. Wang, *et al.*, Single-Phase Mixed Transition Metal Carbonate Encapsulated by Graphene: Facile Synthesis and Improved Lithium Storage Properties, *Adv. Funct. Mater.*, 2018, **28**(10), 1705817.

7 L. Qiu, W. Xiang, W. Tian, et al., Polyanion and Cation Co-Doping Stabilized Ni-Rich Ni-Co-Al Material as Cathode with Enhanced Electrochemical Performance for Li-Ion Battery, Nano Energy, 2019, 63, 103818.

8 Q. B. Zhang, J. X. Wang, J. C. Dong, et al., Facile General Strategy Toward Hierarchical Mesoporous Transition Metal Oxides Array on Three-Dimensional Macroporous Foam with Superior Lithium Storage Properties, Nano Energy, 2015, 13, 77–91.

9 J. S. Yeoh, C. F. Armer and A. Lowe, Transition Metal Oxalates as Energy Storage Materials. A Review, Mater. Today Energy, 2018, 9, 198–222.

10 W. Jin and G. Maduraiveeran, Recent Advances of Porous Transition Metal-Based Nanomaterials for Electrochemical Energy Conversion and Storage Application, Mater. Today Energy, 2019, 13, 64–84.

11 J. H. Li, N. Y. Jiang, J. Y. Liao, et al., Nonstoichiometric $Cu_{0.6}Ni_{0.4}Co_2O_4$ Nanowires as an Anode Material for High Performance Lithium Storage, Nanomaterials, 2020, 10(2), 191.

12 S. Kim, Y. Lim, T. H. Kang, et al., Biotemplated Nanocomposites of Transition-Metal Oxides/Carbon Nanotubes with High Stable and Efficient Electrochemical Interfaces for High-Power Lithium-Ion Batteries, ACS Appl. Energy Mater., 2020, 3(8), 7804–7812.

13 J. K. Miao, D. P. Cai and J. H. Si, Multi-Component Hierarchical Hollow Co-Mo-O Nanocages Anchored on Reduced Graphene Oxide with Strong Interfacial Interfacial Interaction for Lithium-Ion Batteries, J. Alloys Compd., 2020, 828, 154379.

14 M. Michalska, H. J. Xu, Q. M. Shan, et al., Solution Combustion Synthesis of a Nanometer-Scale Co_3O_4 Anode Material for Li-ion Batteries, Beilstein J. Nanotechnol., 2021, 12, 424–431.

15 C. Han, W. Q. Cao and M. S. Cao, Hollow Nanoparticle-Assembled Hierarchical $NiCo_2O_4$ Nanofibers with Enhanced Electrochemical Performance for Lithium-Ion Batteries, Inorg. Chem. Front., 2020, 7(21), 4101–4112.

16 X. S. Tao, Y. Li, H. G. Wang, et al., Multi-Heteroatom-Doped Dual Carbon-Confined Fe_3O_4 Nanospheres as High Capacity and Long-Life Anode Materials for Lithium/Sodium Ion Batteries, J. Colloid Interface Sci., 2020, 565, 494–502.

17 Y. M. Jia, A. M. Cheng, W. Ke, et al., Hierarchical Structure Constructed by Manganese Oxalate Framework with Accurate Iron Doping for Ultra-Efficient Lithium Storage, Electrochim. Acta, 2021, 380, 138217.

18 P. M. Ette, A. Chithambararaj, A. S. Prakash, et al., MoS_2 Nanoflower-Derived Interconnected $CoMoO_4$ Nanoarchitectures as a Stable and High Rate Performing Anode for Lithium-Ion Battery Applications, ACS Appl. Mater. Interfaces, 2020, 12(10), 11511–11521.

19 Y. Huang, X. L. Huang, J. S. Lian, et al., Self-Assembly of Ultrathin Porous NiO Nanosheets/Graphene Hierarchical Structure for High-Capacity and High-Rate Lithium Storage, J. Mater. Chem., 2012, 22(7), 2844–2847.

20 F. Y. Jing, J. Pei, Y. M. Zhou, et al., Hierarchical MnV_2O_4 Double-Layer Hollow Sandwich Nanosheets Confined by N-

Doped Carbon Layer as Anode for High Performance Lithium-Ion Batteries, J. Colloid Interface Sci., 2022, 607, 538–545.

21 Y. F. Zhu, A. P. Hu, Q. L. Tang, et al., Compact-Nanobox Engineering of Transition Metal Oxides with Enhanced Initial Coulombic Efficiency for Lithium-Ion Battery Anodes, ACS Appl. Mater. Interfaces, 2018, 10(10), 8955–8964.

22 S. H. Oh, J. K. Kim, Y. C. Kang, et al., Three-Dimensionally Ordered Mesoporous Multicomponent (Ni, Mn) Metal Oxide/N-Doped Carbon Composite with Superior Li-Ion Storage Performance, Nanoscale, 2018, 10(39), 18734–18741.

23 X. D. Huang, B. Sun, S. Q. Chen, et al., Self-Assembling Synthesis of Free-Standing Nanoporous Graphene-Transition-Metal Oxide Flexible Electrodes for High-Performance Lithium-Ion Batteries and Supercapacitors, Chem.–Asian J., 2014, 9(1), 206–211.

24 Z. Yang, D. Y. Su, J. P. Yang, et al., Fe_3O_4/C Composite with Hollow Spheres in Porous 3D-Nanostructure as Anode Material for the Lithium-Ion Batteries, J. Power Sources, 2017, 363, 161–167.

25 Z. Li, C. Wang, X. Z. Chen, et al., MoOx Nanoparticles Anchored on N-Doped Porous Carbon as Li-Ion Battery, Electrode, 2020, 381, 122588.

26 C. Y. Wang, Y. J. Zhao, L. L. Zhou, et al., Mesoporous Carbon Matrix Confinement Syntheses of Ultrasmall WO_3 Nanocrystals for Lithium Ion Batteries, J. Mater. Chem. A, 2018, 6(43), 21550–21557.

27 C. L. Wang, X. R. Li, Q. Li, et al., Graphene/Co_3O_4 Composites in Application of Electrochemical Energy Conversion and Storage, Flatchem, 2019, 16, 100107.

28 Y. Fu, X. Y. Guo, Z. L. Xu, et al., Nanostructure-Mediated Phase Evolution in Lithiation/Delithiation of Co_3O_4, ACS Appl. Mater. Interfaces, 2021, 13(24), 28171–28180.

29 Y. L. Tan, Q. M. Gao and Z. Y. Li, Unique 1D Co_3O_4 Crystallized Nanofibers with (220) Oriented facets as High-Performance Lithium Ion Battery Anode Materials, Sci. Rep., 2016, 6, 26460.

30 T. I. Lee, J. P. Jegal, J. H. Park, et al., Three-Dimensional Layer-by-Layer Anode Structure Based on Co_3O_4 Nanoplates Strongly Tied by Capillary-Like Multiwall Carbon Nanotubes for Use in High-Performance Lithium-Ion Batteries, ACS Appl. Mater. Interfaces, 2015, 7(7), 3861–3865.

31 Q. Wang, C. Y. Zhang, X. B. Xia, et al., Extremely High Capacity and Stability of Co_3O_4/Graphene Nanocomposites as the Anode of Lithium-Ion Battery, Mater. Lett., 2013, 112, 162–164.

32 D. L. Yan, Y. Zhang, X. Y. Zhang, et al., Co_3O_4 Microtubules Derived from a Biotemplated Method for Improved Lithium Storage Performance, Ceram. Int., 2017, 43(12), 9235–9240.

33 Y. C. Zhao, C. G. Liu, R. W. Yi, et al., Facile Preparation of Co_3O_4 Nanoparticles Incorporating with Highly Conductive MXene Nanosheets as High-Performance Anodes for Lithium-ion Batteries, Electrochim. Acta, 2020, 345, 136203.

34 Y. Fu, H. M. Zhou, Z. H. Hu, et al., Temperature-Induced Microstructure Optimization of Co_3O_4 for the Achievement

of a High-Capacity Carbon Cloth-Based Lithium Ion Battery Anode, *Compos. Commun.*, 2021, **22**, 100446.

35 M. J. Xiao, H. Zhang, B. Zhang, *et al.*, Template-Free Synthesis of a York-Shell Co_3O_4/Nitrogen-Doped Carbon Microstructure for Excellent Lithium Ion Storage, *J. Mater. Chem. A*, 2021, **9**(43), 24548–24559.

36 J. K. Zhu, W. M. Tu, H. F. Pan, *et al.*, Self-Templating Synthesis of Hollow Co_3O_4 Nanoparticles Embedded in N, S-Dual-Doped Reduced Graphene Oxide for Lithium Ion Batteries, *ACS Nano*, 2020, **14**(5), 5780–5787.

37 Y. F. Yuan, F. Chen, L. W. Ye, *et al.*, Construction of Co_3O_4@TiO_2 Heterogeneous Mesoporous Hollow Nanocage-in-Nanocage from Metal-Organic Frameworks with Enhanced Lithium Storage, *J. Alloys Compd.*, 2019, **790**, 814–821.

38 X. Yin, Z. X. Wang, J. X. Wang, *et al.*, One-Step Facile Synthesis of Porous Co_3O_4 Microspheres as Anode Materials for Lithium-Ion Batteries, *Mater. Lett.*, 2014, **120**, 73–75.

39 X. Guan, J. W. Nai, Y. P. Zhang, *et al.*, CoO Hollow Cube/ Reduced Graphene Oxide Composites with Enhanced Lithium Storage Capability, *Chem. Mater.*, 2014, **26**(20), 5958–5964.

40 J. Ayala, D. Ramirz, J. C. Myers, *et al.*, Performance and Morphology of Centrifugally Spun Co_3O_4/C Composite Fibers for Anode Materials in Lithium-Ion Batteries, *J. Mater. Sci.*, 2021, **56**(28), 16010–16027.

41 Y. L. Tan, C. X. Yang, W. W. Qian, *et al.*, Carbon Coated Porous Co_3O_4 Polyhedrons as Anode Materials for Highly Reversible Lithium-Ion Storage, *J. Alloys Compd.*, 2021, **855**(2), 157387.